



Research Article Volume 6 Issue 5 October 2025 DOI: 10.19080/AJOP.2025.06.555697

Academ J Polym Sci

Copyright © All rights are reserved by Wenjuan Zhang

Research on Hollow Sea Urchin-Like Zn-Doped MnO₂ Anode Materials for Lithium-Ion Batteries and Their Modification with GO

Wenjuan Zhang^{1,2}*, Weizu Du^{1,2}, Panpan Zhang^{1,2}, Kangkang Chang^{1,2}, Junfeng Keab Henan Jia^{1,2}, Xudong Bu^{1,2} and Xiujuan Chenc³*

¹School of Materials Science and Engineering, Lanzhou University of Technology, Lanzhou 730050, China

²State Key Laboratory of Advanced Processing and Recycling of Non-Ferrous Metals, Lanzhou University of Technology, Lanzhou 730050, China

³School of Mechanical and Electronical Engineering, Lanzhou University of Technology, Lanzhou 730050, China

Submission: October 01, 2025; Published: October 14, 2025

*Corresponding author: Wenjuan Zhang, School of Mechanical and Electronical Engineering, Lanzhou University of Technology, Lanzhou 730050, China

Abstract

This study reports on a GO-modified Zn-doped hollow sea urchin-like MnO_2 anode material for lithium-ion batteries. Firstly, Zn/MnO2 anode materials with varying Zn^{2+} doping levels were prepared using the hydrothermal method. Then, by combining different amounts of graphene oxide with Zn/MnO_2 , it was found that when the graphene oxide content is 20% (referred to as the GO-20 anode material), the composite exhibits specific capacity, stability, and better rate performance. After 100 cycles at a current density of 0.1 C, the discharge specific capacity reached 920.9 mA h g^{-1} , and the charge specific capacity reached 915.3 mA h g^{-1} , with a coulombic efficiency of 99.39%. These results demonstrate that appropriate doping and composite modification can significantly enhance the electrochemical performance of MnO2 materials. The combination of graphene and nanocomposite materials provides more active sites and a more stable structure, contributing to increased energy density and cycle stability of the battery.

Keywords: Energetic Material; Composite Materials; Electrical Properties

Introduction

As traditional non-renewable energy reserves decrease, the world is seeking more reliable ways to develop energy to sustain operations in industries and automobiles, among others [1-3]. To provide a safe and sustainable alternative to resources, scientists and engineers are dedicated to the utilization and development of renewable energy and energy storage [4,5]. Batteries, as devices that convert chemical energy into electrical energy, can safely store renewable energy. Batteries have exceeded expectations and have become a reliable application choice in fields beyond military, aerospace, and commercial electronic devices. The continuous development of rechargeable batteries has improved performance in aspects such as mobility and energy density [6-10]. Since Volta [11] invented the voltaic pile in 1800, the development of chemical power sources has spanned over 200 years. Currently, the main types of batteries include nickel-metal

hydride batteries, fuel cells, lead-acid batteries, supercapacitors, and lithium-ion batteries. Among them, lithium-ion batteries are recognized as the preferred energy storage devices due to their high energy density, stable transmission, and low cost [12-14]. Lithium-ion batteries are widely noted for their high energy density, high power density, no memory effect, and environmental friendliness, and they are used in various fields.

The performance of lithium-ion batteries depends on the performance of components such as the anode material, cathode material, electrolyte, and separator [15,16]. As one of the key components of lithium-ion batteries, the optimization of anode materials will directly enhance the overall performance of the battery [17]. Currently, graphite materials are widely used in commercial lithium-ion battery anodes. However, the low theoretical specific capacity of graphite materials (372 mA h g⁻¹)

[18-24] and poor rate performance cannot meet the demand for higher electrochemical performance in practical applications. Manganese dioxide (MnO₂), with a theoretical capacity of 1230 mA h g-1, is considered an ideal material for lithium batteries due to its environmental friendliness and low cost. Different combinations of the manganese-oxygen octahedral [MnO₆] units can form various crystalline forms (such as α , β , γ , λ etc.) and morphologies (such as nanospheres, nanowires, nanocubes, nanotubes, etc.) of manganese dioxide [25]. For instance, Wu [26] and colleagues prepared Zn-doped MnO2 ultrathin nanosheets with abundant defects for use as anode materials in lithium-ion batteries. Jia [27] and colleagues synthesized Zn-doped SnO₂ dendritic hierarchical cubic structures for lithium-ion battery anodes. Tang [28] and colleagues achieved high durability of δ-MnO₂-based pseudocapacitive electrodes by Zn doping-induced reattachment, for use in lithium-ion battery anodes. Hao [29] and colleagues used a simple hydrothermal method to synthesize Ni-doped MnO2 nanoneedles as anode materials for lithium-ion

By doping with metal ions, specific defect structures can be formed within the electrode material, providing new ion storage sites that accelerate the electrochemical reaction speed. These defect sites not only enhance the ion storage capacity of the electrode materials but also improve their cycling stability [30-33]. The presence of defect sites helps to diminish volume changes during charge and discharge cycles, reducing cracks and fractures in the material, thus enhancing its cycle stability [34]. In addition, incorporating highly conductive carbon materials such as graphene, activated carbon, and carbon nanotubes can effectively enhance the conductivity of the material. For example, Cetinkaya et al. [35] prepared graphene/α-MnO₂ nanocomposite cathodes using ultrasonic and mechanical alloying equipment, proving that graphene enhanced the electrochemical reactions of α -MnO₂ and improved the material's conductivity. Khan et al. [36] grew sea urchin-shaped MnO, nanowires directly on carbon microfibers (MGC) mats coated with porous reduced graphene oxide, resulting in batteries with excellent rechargeability and rate performance. Zhang et al. [37] used a traditional hydrothermal method to prepare high-performance MnO2 nanocomposites (GMC), showing that GMC nanocomposites have great potential in lithium-ion batteries.

Yu et al. [38] used ultrafiltration technology to prepare monolayer-assembled graphene- MnO_2 nanotube (NT) films and studied their performance as anodes for lithium-ion batteries, demonstrating excellent cycling and rate capabilities. Research has shown that the addition of graphene provides highly conductive interconnections, facilitating easier electron propagation during charge/discharge processes, thereby enhancing ion absorption capacity and increasing rate performance. Additionally, graphene can prevent the detachment of protective coating materials during cycling and improve the conductivity, structural stability, and lithium-ion transport efficiency of electrode materials, significantly enhancing their reversible specific capacity, rate

performance, and cycle life, among other electrochemical properties [39, 40]. In this study, hollow sea urchin-like $\rm MnO_2$ was selected as the anode material. Physical characterization and electrochemical performance tests were conducted to evaluate hollow sea urchin-like $\rm MnO_2$ anode materials with different $\rm Zn^{2+}$ doping levels, aiming to determine the optimal doping content. Furthermore, the material was modified by doping with graphene oxide (GO) to achieve higher performance.

Results and Discussion

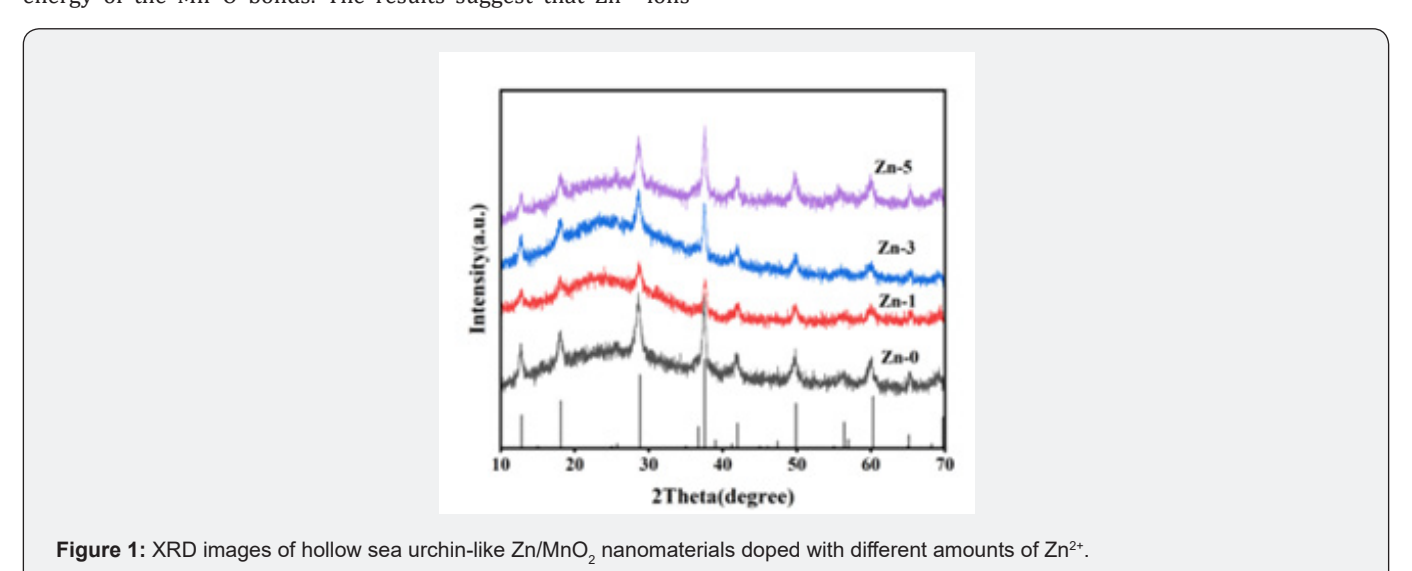
Zn/MnO₂ doping modification

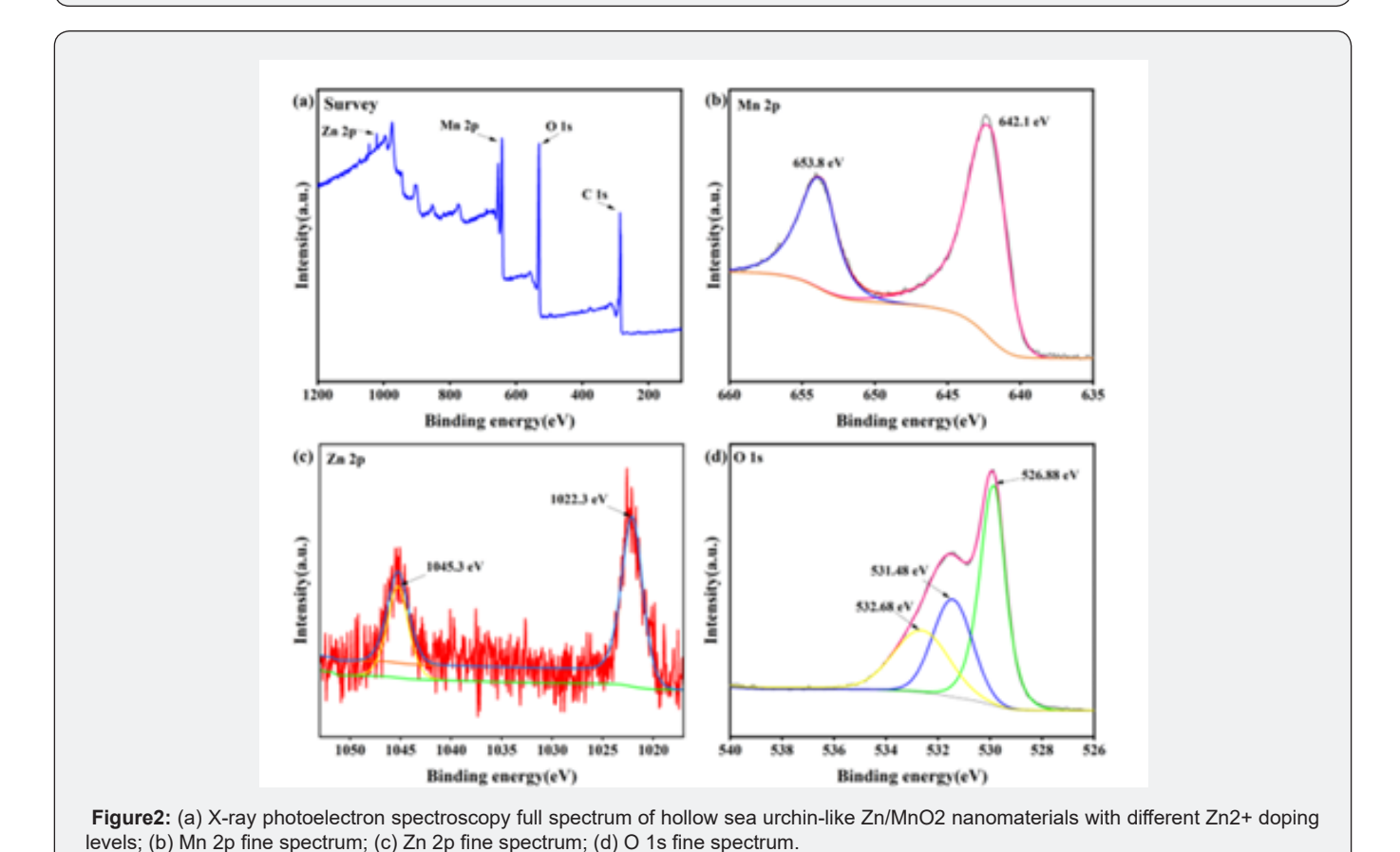
In order to study the crystal structure and composition of zinc-doped MnO₂ materials, X-ray diffraction (XRD) analysis was conducted on the synthesized samples. As shown in (Figure 1), it can be seen that the different amounts of zinc doping do not increase or decrease the diffraction peaks; these peaks correspond perfectly to the tetragonal α-MnO₂ phase (JCPDS#44-0141). All preferred diffraction peaks correspond one-to-one to the crystal planes at 12.7°, 18.1°, 28.8°, 37.5°, 42.1°, 49.9°, 56.2°, and 60.3°, which are (110), (200), (310), (211), (301), (411), (600), and (521) respectively [41]. These crystal planes are formed by the random coexistence of (1×1 tunnel) and (2×2 tunnel) crystal structures [42]. With this tunnel crystal structure, the electronic conductivity of the host can be increased, and the Li* diffusion rate can be enhanced [43]. After the incorporation of Zn, no characteristic peaks of zinc oxide or metallic zinc were found, confirming that the synthesized doping product is pure, suggesting that zinc ions may have entered the MnO₂ lattice. Furthermore, after doping Zn into MnO₂, the XRD pattern still maintains the α-type structure; however, compared to the undoped material, the characteristic diffraction peaks of Zn/α -MnO₂ show a slight shift to the right, indicating a change in the crystal structure of α -MnO₂. This is because the ionic radius of Zn²⁺ (0.74 Å) is larger than that of Mn⁴⁺ (0.67 Å), and the substitution of Mn⁴⁺ by Zn²⁺ leads to distortion of the crystal structure. As the content of Zn²⁺ increases, the intensity of the diffraction peaks also decreases, indicating that Zn²⁺ has been successfully incorporated into the hollow sea urchin-like α-MnO₂ nanomaterials.

In order to investigate the valence states of elements in the synthesized $\rm Zn/MnO_2$ nanomaterials and the chemical bonds within the material, X-ray photoelectron spectroscopy (XPS) analysis was conducted on the doped materials. (Figure 2a) shows the full spectrum of the photoelectrons for the doped material, revealing the presence of four elements: Mn, Zn, C, and O, indicating that Zn atoms have been successfully doped into MnO². As shown in (Figure 2b), the high-resolution Mn 2p spectrum exhibits two peaks at 642.1 eV and 653.8 eV, with a spin-orbit splitting of 11.7 eV, corresponding to the Mn 2p3/2 and Mn 2p1/2 orbitals, respectively, which is in good agreement with previously reported literature [44]. This indicates that the addition of $\rm Zn^{2+}$ ions into the MnO² lattice reduces the binding energy of the Mn–O bonds. According to (Figure 2c), the Zn 2p spectrum shows two peaks with binding energies of 1045.3 eV and 1022.3 eV, corresponding

to the Zn 2p1/2 and Zn 2p3/2 orbitals, respectively, indicating that the valence state of zinc is predominantly divalent [22]. (Figure 2d) presents the fine spectrum of O 1s, showing three peaks at 526.88 eV, 531.48 eV, and 532.68 eV, with the peak at 526.8 eV corresponding to oxygen atoms in MnO $_2$ existing in the O $_2$ - valence state, which relates to the Mn-O-Mn bond. Compared to undoped $\alpha\text{-MnO}_2$, the binding energy is decreased, indicating that the addition of Zn $^{2+}$ ions into the MnO $_2$ lattice lowers the binding energy of the Mn-O bonds. The results suggest that Zn $^{2+}$ ions

entering the α -MnO $_2$ lattice substitute some Mn⁴⁺ ions, creating Mn⁴⁺ vacancies in the lattice to maintain electrostatic balance [30]. These Mn⁴⁺ vacancies are beneficial for enhancing the diffusion of Li⁺ ions in the MnO $_2$ material, thus positively impacting the rate capability. Furthermore, incorporating Zn²⁺ as a low-valence cation into manganese oxides can significantly enhance the resultant electrochemical performance by constructing oxygen vacancies [45].





How to cite this article: Wenjuan Z, Weizu D, Panpan Z, Kangkang C, Junfeng Keab Henan J, et al. Research on Hollow Sea Urchin-Like Zn-Doped MnO₂ Anode Materials for Lithium-Ion Batteries and Their Modification with GO. Academ J Polym Sci. 2025; 6(5): 555697. DOI: 10.19080/AJ0P.2025.06.555697

The morphology of the $\rm Zn/MnO_2$ nanomaterials was further characterized using scanning electron microscopy (SEM). (Figure 3) presents the SEM images of four samples: Zn-0, Zn⁻¹, Zn⁻³, and Zn⁻⁵. It can be observed from (Figure 3a, 3b & 3d) that all samples exhibit a complete urchin-like appearance of Zn/MnO $_2$ nanoparticles. When there is no Zn²⁺ doping, the spines of the hollow sea urchin-like Zn/MnO $_2$ nanomaterials are relatively smooth. With doping, a layer of fuzzy material appears on the sample's surface, and as the doping level increases, the fuzziness on the surface becomes more pronounced, leading to increased

surface roughness. When there is an excess of zinc ions, the doped zinc ions may diffuse to the surface of the sample, reducing the diffusion efficiency of Li * and consequently affecting the battery's conductivity. (Figure 3c) shows the SEM image of the Zn $^{-3}$ sample, where the sample is observed to be uniformly distributed with uniform particle size. In summary, a larger specific surface area of the sample provides more reactive sites, accelerating the electrochemical reactions and overcoming the inherently low conductivity of MnO $_2$ nanomaterials.

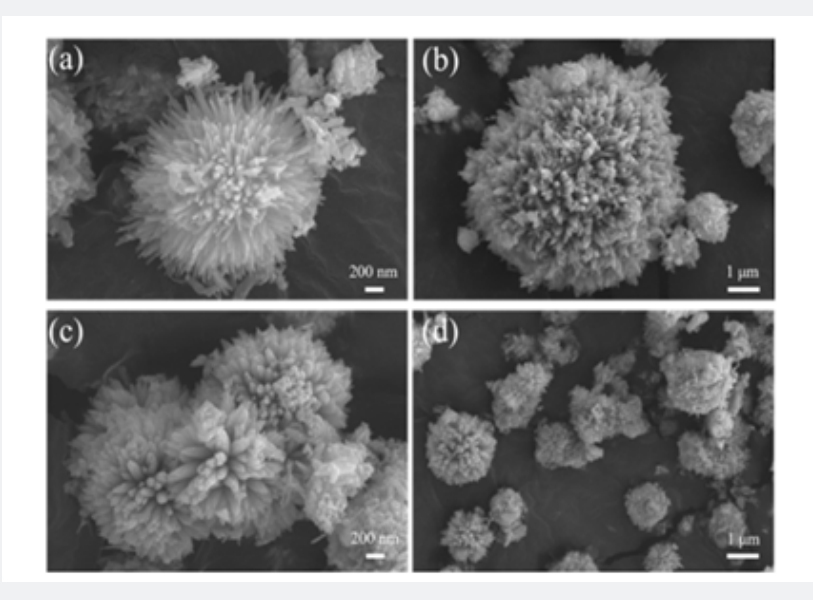


Figure 3: SEM images of hollow sea urchin-like Zn/MnO2 nanomaterials with different Zn²⁺ doping levels (a) Zn⁻⁰; (b) Zn⁻¹; (c) Zn⁻³; (d) Zn⁻⁵.

Meanwhile, the elemental composition and distribution of the hollow sea urchin-like Zn⁻³/MnO₂ nanomaterials were analysed using EDS spectrometry, and the results are shown in (Figure S1). The EDS elemental distribution test revealed that the sample contains three elements: 0, Mn, and Zn, which is consistent with the XPS analysis results. It was also found that the three elements are distributed relatively uniformly within the particles. These results indicate that the synthesized Zn-3/MnO₂ nanomaterials have high purity, with the Zn element evenly distributed throughout the Zn-3/MnO₂ nanomaterials, in agreement with the XRD analysis results. (Table S1) shows the distribution of elements in Zn-3/MnO₂, where the atomic percentages of O, Mn, and Zn in the Zn-3/MnO₂ anode material are 59.09%, 31.82%, and 9.09%, respectively. The mass percentages of the three elements are 33.95%, 58.36%, and 9.09%, respectively. This indicates that Zn has been successfully doped into the hollow sea urchin-like MnO₂ nanomaterials, resulting in a high-purity product without the presence of other elements. To investigate the cycling stability of hollow sea urchin-like Zn/MnO2 nanomaterials with different Zn²⁺ doping levels as anode materials for lithium-ion batteries, and the performance enhancement due to doping modification, the cycling performance of four samples with varying Zn²⁺ doping levels was tested at a current density of 0.1 C.

The comparison results are shown in (Figure 4). From the (Figure 4), it can be observed that the initial charge capacity, discharge capacity, and coulombic efficiency for Zn-0, Zn-1, Zn-3, and Zn-5 are 1202.6 mA h g⁻¹, 1723.4 mA h g⁻¹, 69.78%; 1104.5 mA h g⁻¹, 1606.08 mA h g⁻¹, 68.77%; 1398.6 mA h g⁻¹, 1856.7 mA h g⁻¹, 75.33%; and 1231.1 mA h g⁻¹, 1789.4 mA h g⁻¹, 68.8%, respectively. It can be seen that the three doped samples have higher initial charge capacity, discharge capacity, and coulombic efficiency than the undoped Zn-0 electrode material. The Zn ion doping effectively buffers the volume changes of the electrode material during charge and discharge, resulting in improved electrochemical performance and structural stability. After 100 cycles, the Zn-3/MnO₂ electrode material shows higher charge and discharge capacities compared to the other three electrode materials, at 705.8 mA h $\rm g^{-1}$ and 707.6 mA h $\rm g^{-1}$, respectively, with a coulombic efficiency of 99.75%. The lower initial coulombic efficiency is due to the formation of a solid electrolyte interface (SEI) film and some irreversible Li20 during the first discharge, leading to significant lithium loss. However, the doping creates more Li⁺ contact points, which aids in Li⁺ storage and promotes the

material's reversible reactions, enhancing the battery's stability. These studies demonstrate that doping modification effectively promotes reversible reactions during charging and discharging and improves the cycling stability of the material. Compared to the $\rm Zn^{-0}$ electrode material, the $\rm Zn^{-3}$ electrode material better

mitigates capacity decline, indicating that Zn^{-3} electrode material possesses excellent electrochemical performance, suggesting that an appropriate amount of Zn ion doping in hollow sea urchin-like Zn^{-3}/MnO_2 electrode materials results in a more stable structure.

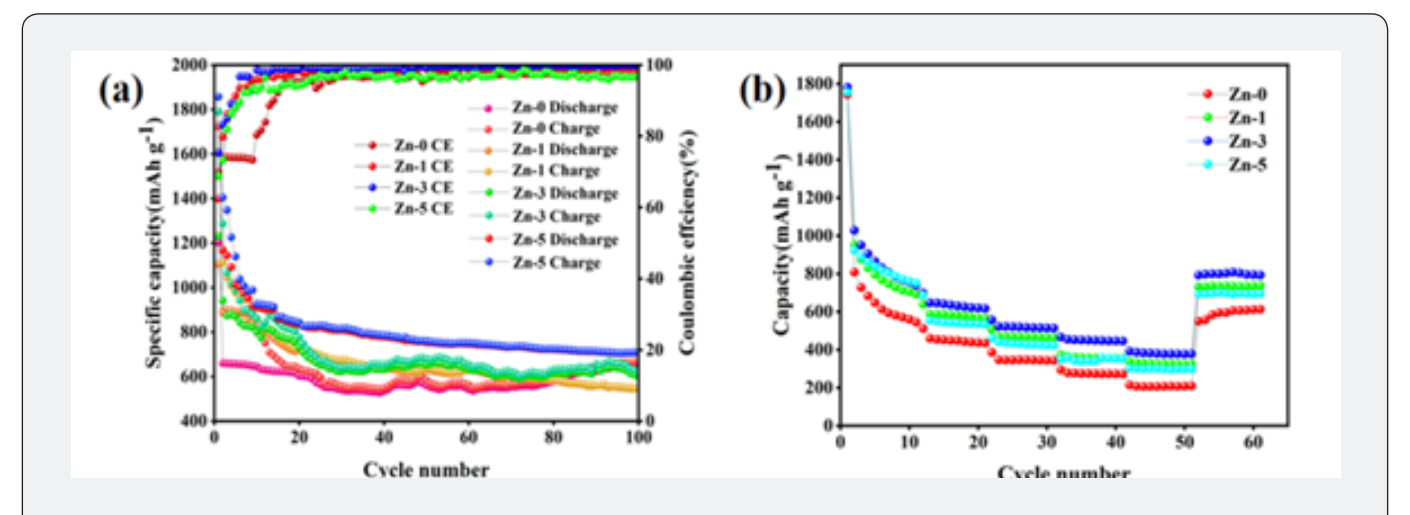


Figure 4: (a) Cycling performance of hollow sea urchin-like Zn/MnO2 electrode materials with different Zn2+ doping levels at a current density of 0.1 C; (b) Rate performance of hollow sea urchin-like Zn/MnO2 electrode materials with different Zn2+ doping levels at various current densities.

By testing the cycling performance of the Zn/MnO₂ electrode materials at different current densities, the rate performance was further studied. (Figure 4b) shows the rate performance of the synthesized Zn-0, Zn-1, Zn-3, and Zn-5 electrode materials. It can be observed that when used as anodes for lithium-ion batteries, the Zn-3 electrode material exhibits average discharge capacities of 865.7 mA h g^{-1} , 641.4 mA h g^{-1} , 520.7 mA h g^{-1} , 451.3 mA h $g^{-1}\text{,}$ and 382.4 mA h g^{-1} at current densities of 0.1 C, 0.2 C, 0.5 C, 1.0 C, and 2.0 C, respectively. Additionally, when the current density is restored from 2.0 C to 0.1 C, the discharge capacity of the Zn-3 electrode material quickly recovers to 799.6 mA h g⁻¹. In contrast, for the Zn-0 electrode material, the average discharge capacities are 647.7 mA h g⁻¹, 452.5 mA h g⁻¹, 346.5 mA h g⁻¹, 274.9 mA h g⁻¹, and 206.7 mA h g⁻¹ at the same current densities, and the discharge capacity recovers to 594.8 mA h g⁻¹ at 0.1 C, indicating that Zn-0 has a lower recovery compared to the Zn-3 electrode material. As seen in (Figure 4b), the doped samples exhibit higher performance at all current densities compared to the Zn⁻⁰ electrode material, suggesting that the zinc ion doping somewhat buffers the volume strain during repeated chargedischarge cycles. From the comparison of the rate performance curves of hollow sea urchin-like Zn/MnO2 electrode materials with different Zn²⁺ doping levels, it is evident that the synthesized Zn-3 sample demonstrates excellent cycling and rate performance when used as the anode material for batteries.

The application of cyclic voltammetry (CV) curves helps to gain an in-depth understanding of the reaction mechanisms of

the Zn⁻³ anode material during the charging and discharging processes. Therefore, cyclic voltammetry tests were conducted on the Zn-3 anode within a voltage range of 0.01-3.0 V and at a scan rate of 0.1 mV s⁻¹. (Figure 5a) shows the CV curves for the first three cycles. As the voltage decreases during the cathodic sweep of the first cycle, three reduction peaks appear at 0.5 V, 1.2 V, and 2 V. These peaks represent the formation of a Zn/MnO₂ solid solution from MnO₂, the formation of Mn2O3, the formation of Mn nanoparticles dispersed in the lithium matrix Li20, and the formation of a solid electrolyte interface (SEI) film due to the irreversible decomposition of the electrolyte. The oxidation peak observed at 1.2 V corresponds to the partial oxidation of Mn to Mn2O3, Zn/MnO2, and MnO2 substances, a process described by (equation 1). The significant differences observed between the first and second cycles when transition metal oxides are used as anodes can be attributed to the lithiation of lithium ions and the formation of the SEI layer on the electrode material surface [46]. The similarity of the CV curves in the second and third cycles indicates the stability and reversibility of the Zn-3 electrode material [47].

$$MnO_2 + 2Li^+ + 2e^- \leftrightarrow Mn + Li_2O$$
 (1)

To further investigate the charge-discharge processes of the ${\rm Zn^{-3}}$ anode material, charge-discharge tests were conducted within a voltage range of 0–3 V at a current density of 0.1 C. The charge-discharge curves for the first three cycles are shown in (Figure 5b). Comparing with the CV curves in (Figure 5a), the voltage plateaus in the charge-discharge curves correspond to the peaks in the CV

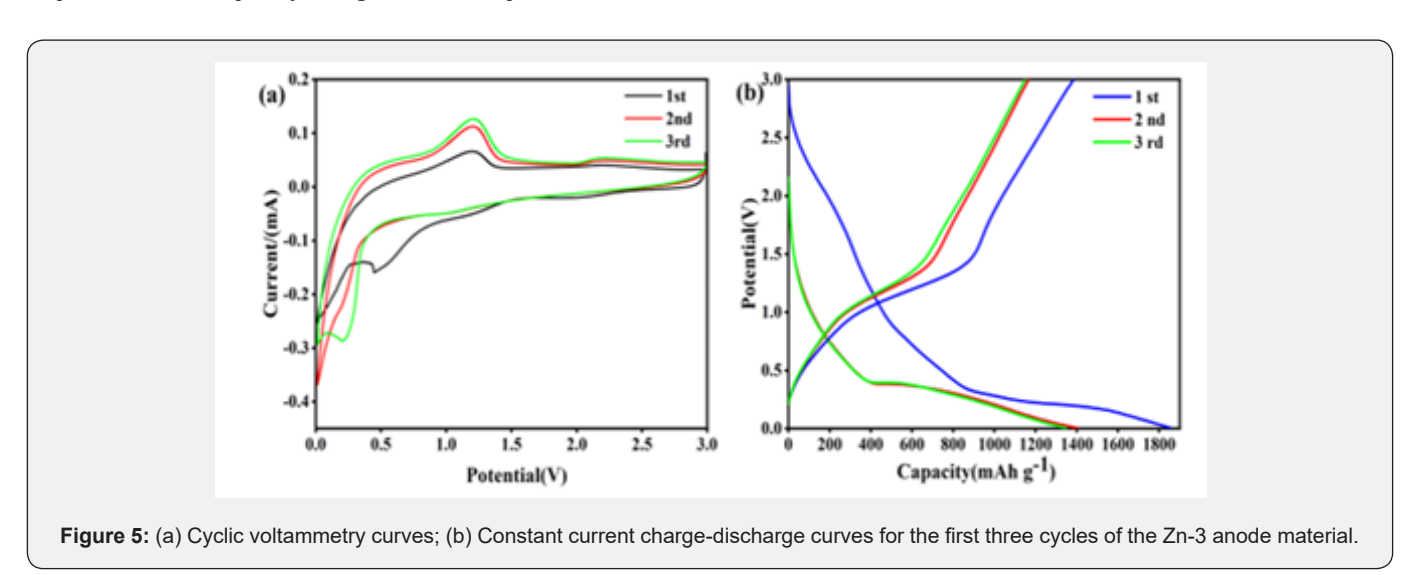
curves, further validating the reaction mechanisms of $\rm Zn^{-3}$ during the charge-discharge process. Additionally, it was found that the initial charge-discharge specific capacity and coulombic efficiency of the $\rm Zn^{-3}$ anode material are 1398.6 mA h g⁻¹ and 1856.7 mA h g⁻¹, and 75.32%, respectively. The irreversible decomposition of the electrolyte in the $\rm Zn^{-3}$ anode material results in the formation of a substantial amount of SEI film on the material's surface, leading to capacity loss. The accumulation of some irreversible amorphous $\rm LiO_2$ also causes significant lithium loss [48].

To explore the fundamental reasons for the improved kinetic performance of the Zn⁻³/MnO₂ electrode material, we conducted a comparative study of the charge transfer properties of Zn⁻⁰ and Zn⁻³ electrode materials using electrochemical impedance spectroscopy (EIS). (Figure S2) presents the impedance spectra, where it is observed that the impedance curves for both Zn⁻⁰ and Zn⁻³ electrode materials consist of a high-frequency semicircle and a low-frequency straight line. The high-frequency semicircle represents the charge transfer resistance between the electrode material and the liquid electrolyte [49], while the low-frequency straight line reflects the diffusion resistance of Li⁺ in the electrolyte [50,51]. A clear observation from (Figure S2) shows that the diameter of the high-frequency semicircle for the Zn⁻³ electrode material is smaller than that of the Zn⁻⁰ electrode material, and the slope of the low-frequency straight line is steeper. This indicates

that Zn^{-3} has lower charge transfer resistance and Li^{+} diffusion resistance, allowing smoother charge transfer. Therefore, the incorporation of zinc ions significantly reduces the charge transfer resistance of the Zn^{-0} electrode material, increases its conductivity, and improves its electrochemical performance.

Zn-3/MnO₂@GO doping modification

To investigate the crystal structure and phase composition of the Zn⁻³/MnO₂@GO composite material, the X-ray diffraction (XRD) pattern of the Zn⁻³/MnO₂@GO composite material was measured and is shown in (Figure 6). Similar to (Figure 1), only the tetragonal α -MnO $_2$ phase (JCPDS#44-0141) can be observed. The diffraction peaks at 12.7°, 18.1°, 28.8°, 37.5°, 42.1°, 49.9°, 56.2°, and 60.3° correspond to the crystal planes (110), (200), (310), (211), (301), (411), (600), and (521), respectively. No other diffraction peaks are observed, indicating the absence of additional impurity phases in the material. Moreover, the intensity of the diffraction peaks decreases, and the peaks gradually broaden, but the peak tops remain sharp. This suggests that the crystal structure of Zn-3/MnO₂ has not significantly changed after being combined with graphene oxide, indicating that the material's crystallinity is still high. No diffraction peaks of graphene are observed in the XRD pattern, indicating that the graphene oxide in the composite material is in an amorphous form.

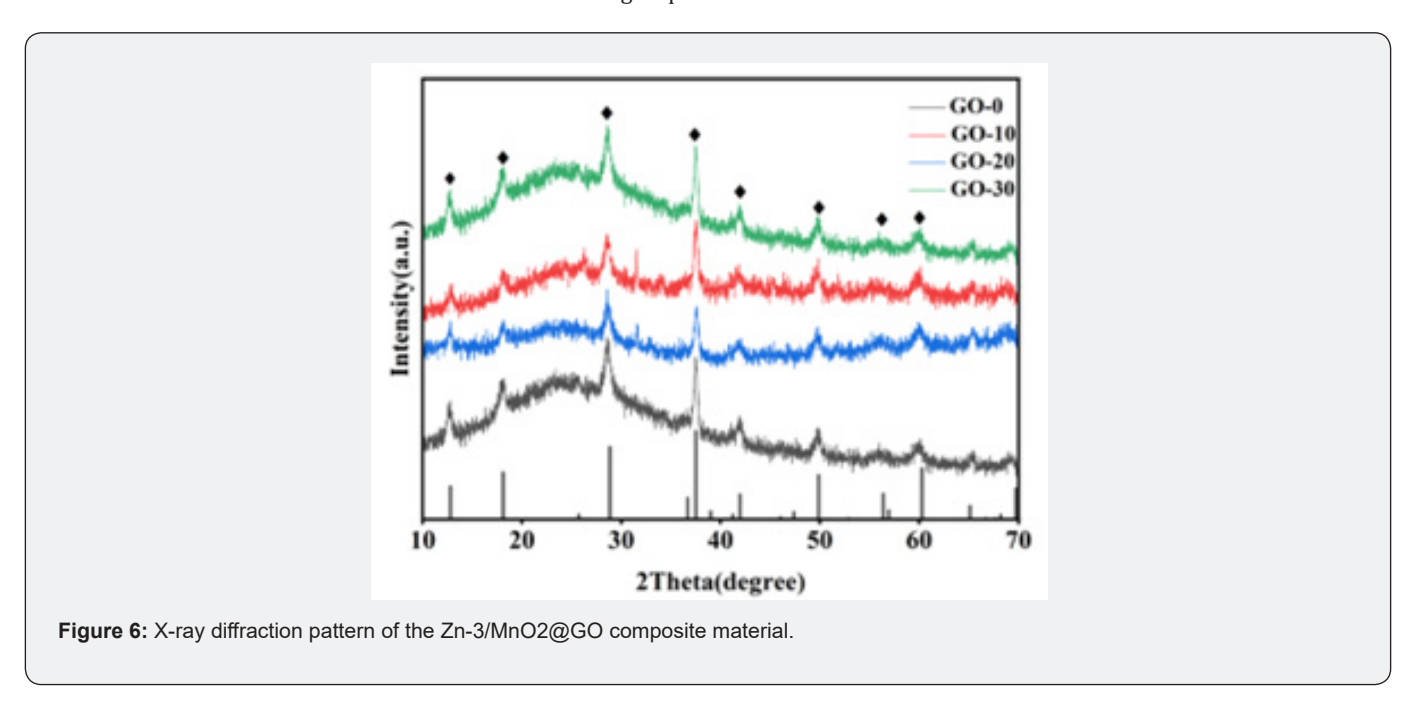


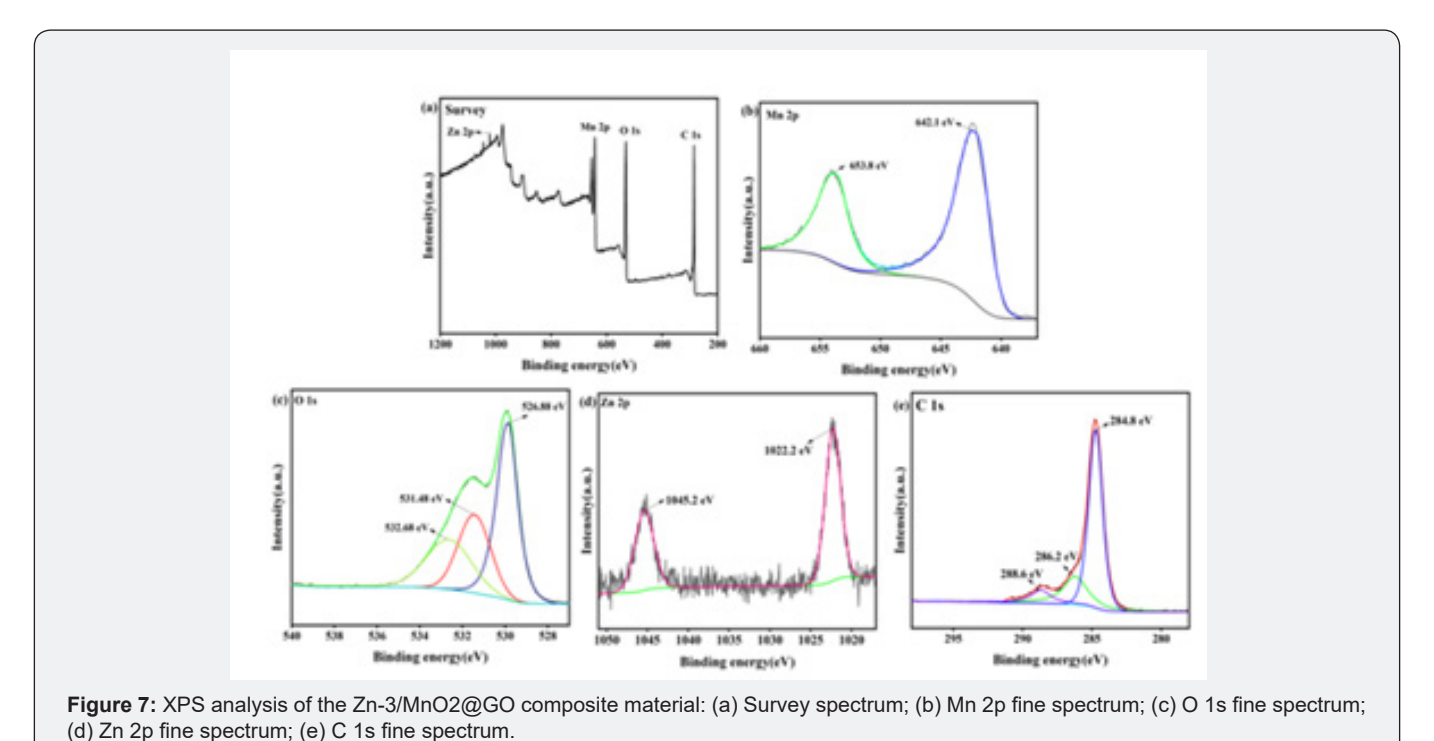
To further investigate the composition and chemical valence states of the $\rm Zn^{-3}/MnO_2@GO$ composite material, X-ray photoelectron spectroscopy (XPS) analysis was conducted, as shown in (Figure 7). The survey spectrum in (Figure 7a) reveals the presence of four elements: Mn, O, Zn, and C, which are further analyzed through their fine spectra. As shown in (Figure 7 b), the Mn 2p spectrum exhibits two fitted peaks at 642.1 eV and 653.8 eV, corresponding to the Mn 2p3/2 and Mn 2p1/2 orbitals, respectively. These peaks are consistent with the electron state of Mn4 $^+$ [52]. In (Figure 7c), the oxygen peak remains unchanged,

confirming the presence of $\rm O_2^-$ in the material and indicating that the carbon coating is only on the surface of the sea urchinlike structure without altering the crystal structure. (Figure d) presents the Zn 2p spectrum, which shows two fitted peaks at binding energies of 1022.2 eV and 1045.2 eV, corresponding to Zn 2p3/2 and Zn 2p1/2 orbitals, respectively. This suggests that the valence state of zinc ions remains unchanged by the graphene oxide, further confirming the presence of Zn2* in the composite material. In (Figure 7e), the C1s fine spectrum displays three fitted peaks at 284.8 eV, 286.2 eV, and 288.6 eV. These binding energies

correspond to C-C, C-O, and C=O chemical bonds, respectively. The C-C bond is the main chemical bond in the graphene structure, while the C-O and C=O bonds are related to the functional groups

on the surface of graphene oxide, indicating the presence of graphene oxide [53].





A detailed study of the morphology of the $\rm Zn^{-3}/MnO_2@GO$ composite material was conducted using scanning electron microscopy, as shown in (Figure 8). It was observed that the content of graphene oxide affects the morphology of the samples. With an increase in graphene content, a layer of material appeared to wrap around the sea urchin-like spikes on the sample surface.

(Figure 8a) shows that in samples without graphene oxide, the spacing between the sea urchin-like spikes is relatively large, but it decreases after the incorporation of graphene oxide. In (Figure 8b), high-magnification SEM images reveal that the samples retain their sea urchin-like morphology, with each spike coated with a layer of graphene oxide, indicating that there is no agglomeration

of particles. The hollow sea urchin-like nanoparticles possess a large specific surface area, and their combination with graphene oxide further increases the specific surface area of the composite material. This enhancement accelerates the electrochemical reaction rate to some extent and provides more active sites for the reactions. Due to the structural stability and good conductivity

of graphene oxide, when nanoparticles are evenly dispersed on its surface, the composite material, using graphene oxide as a framework, benefits from improved stability and conductivity. Additionally, it helps prevent the aggregation of nanoparticles, thereby enhancing the cycling stability and kinetic performance of lithium-ion batteries.

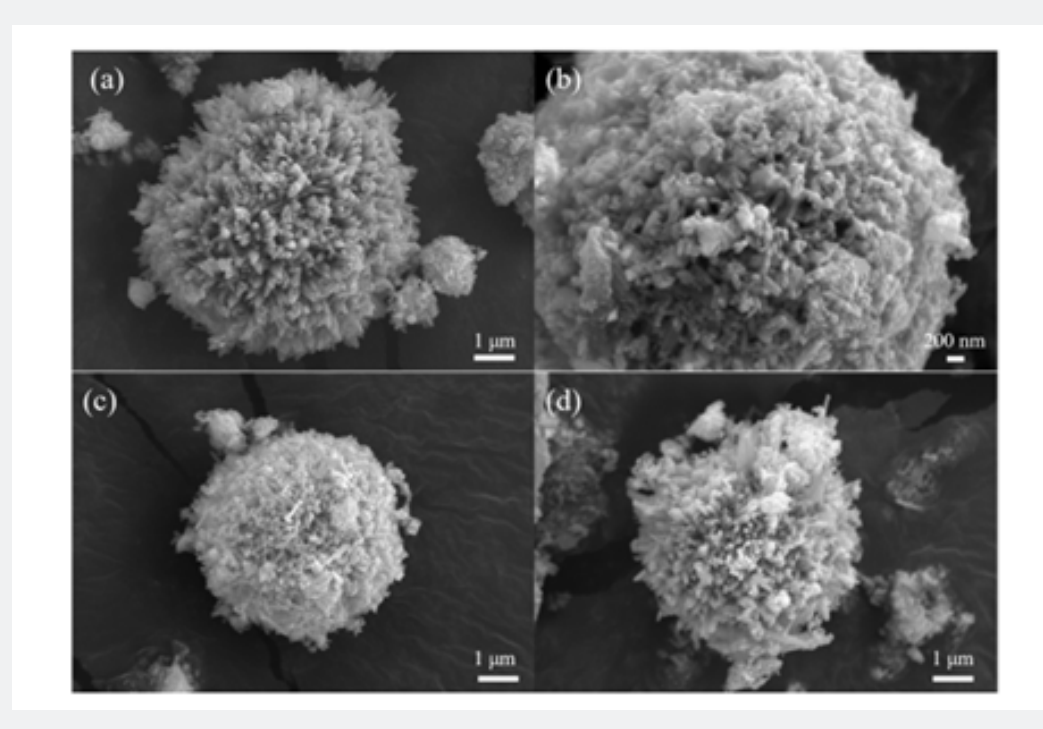


Figure 8: SEM images of the Zn-3/MnO2@GO composite material: (a) GO-0; (b) GO-10; (c) GO-20; (d) GO-30.

The composition and distribution of elements in the composite material were studied using EDS spectroscopy. As shown in (Figure S3), four elements- C, O, Mn, and Zn-are present in the composite. The elements O, Mn, and Zn are distributed only within the nanoparticles, and each element is distributed relatively uniformly. The element 0 is found only on the surface of the sample, specifically in the single-layer graphene. (Figure S3d) reveals that the sea urchin-like structure is hollow, which indirectly confirms the successful preparation of the hollow sea urchin-like MnO2 nanomaterials. The intensity of the elements O, Mn, and Zn gradually decreases, which corresponds to their varying concentrations in the composite material. The EDS analysis further confirms the successful incorporation of graphene oxide with Zn-3/MnO₂. The varying content of graphene oxide in the composite materials results in differences in their electrochemical performance. By comparing the cycling performance and charge-discharge specific capacity of composites with different graphene oxide contents, the optimal graphene oxide content can be determined. (Figure 9a) shows the cycling efficiency and Coulombic efficiency of composites with various graphene oxide

contents over 100 cycles at a current density of 0.1 C. The initial discharge specific capacities for the GO-0, GO-10, GO-20, and GO-30 samples are 1856.7 mA h g-1, 1816.9 mA h g-1, 1894.7 mA h g-1, and 1845.3 mA h g-1, respectively. The GO-20 electrode material demonstrates a better initial discharge specific capacity than the other samples, indicating that the graphene oxide content is not directly proportional to the electrochemical performance of the battery.

Only with an appropriate amount of graphene does the conductivity of the electrode material increase, thereby enhancing charge-discharge performance. The initial charge specific capacities for GO-0, GO-10, GO-20, and GO-30 samples are 1398.6 mA h g^-1, 1312.4 mA h g^-1, 1396.5 mA h g^-1, and 1320.4 mA h g^-1, with capacity retention rates of 75.33%, 72.23%, 73.71%, and 71.55%, respectively. It appears that the introduction of graphene does not improve capacity retention; however, after 15 cycles, the charge-discharge specific capacity of the GO-20 sample exceeds that of the other samples, declining less and maintaining stability throughout the cycling process, indicating that the GO-20 sample has superior stability compared to the others. After 100 cycles, the

discharge specific capacity of the GO-20 sample remains around 920.9 mA h g $^{-1}$, with a charge specific capacity of 915.3 mA h g $^{-1}$ and a Coulombic efficiency of 99.39%, all higher than those of the other samples. Additionally, the cycling curve of the GO-20 sample after 20 cycles is more stable than that of the other samples. Throughout prolonged cycling, the capacity of the GO-20 sample shows no significant degradation. As the graphene oxide content

increases, the proportion of MnO_2 decreases. Since the theoretical specific capacity of MnO_2 is higher than that of graphene, the capacity of the composite material may decrease. After 100 cycles, it is observed that the GO-20 anode material has a higher reversible specific capacity than the other anode materials. The stability of the GO-20 anode material during charge-discharge cycles suggests that the cycling performance of GO-20 is optimal.

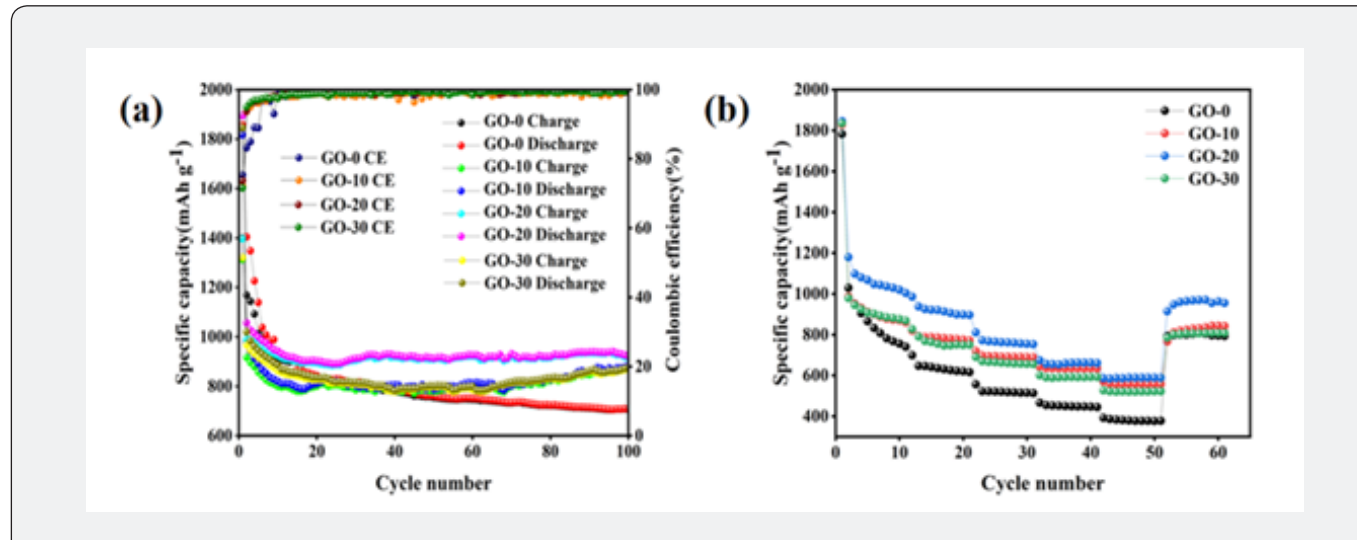


Figure9(a): Cycling performance curves of Zn-3/MnO2 anodes with varying graphene content; (b): Rate performance curves of Zn-3/MnO2 anodes with varying graphene content.

To understand the impact of graphene oxide composite modification on the rate performance of materials, rate performance tests were conducted on four samples. (Figure 9b) shows the rate performance test curves for the four samples at different current densities of 0.1 C, 0.2 C, 0.5 C, 1 C, and 2 C. The average discharge specific capacities of the GO-0 composite at current densities of 0.1 C, 0.2 C, 0.5 C, 1.0 C, and 2.0 C are 832.4 $mA h g^{-1}$, 636.7 $mA h g^{-1}$, 519.7 $mA h g^{-1}$, 450.2 $mA h g^{-1}$, and 380.5 mA h g⁻¹, respectively. When the current density returns from 2.0 C to 0.1 C, its discharge specific capacity quickly recovers to 803.3 mA h g-1. In contrast, the GO-20 anode has average discharge specific capacities of 900.4 mA h g-1, 785.4 mA h g-1, 691.7 mA h g-1, 634.7 mA h g-1, and 558.7 mA h g-1 at current densities of 0.1 C, 0.2 C, 0.5 C, 1.0 C, and 2.0 C, respectively. When the current density returns from 2.0 C to 0.1 C, its discharge specific capacity quickly recovers to 828.7 mA h g⁻¹. Clearly, the rate performance of GO-20 is significantly higher than that of GO-0, and the rate performance of the GO-20 electrode material is also superior to that of other graphene oxide composite samples. This result can be attributed to the excellent conductivity and ion diffusion performance of graphene oxide. The introduction of graphene oxide effectively enhances the ionic and electronic conductivity of the composite material, significantly improving the kinetic performance of the electrode material. In batteries, the migration rates of ions and electrons are crucial for the charge-discharge rate of the electrodes. Therefore, optimizing the conductivity

of composite materials can significantly improve the chargedischarge performance and cycling stability of batteries.

To investigate the reaction mechanism of the GO-20 electrode material during charge and discharge processes, CV curves of the GO-20 electrode material were tested at a scan rate of 0.2 mV s⁻¹ over a scan range of 0.01 to 3.0 V. The CV curves for the first three cycles are shown in (Figure 10 a). As the voltage decreases, two reduction peaks appear at 2.23 V and 0.62 V, respectively. The reduction peak at 2.23 V represents the formation of Zn/ MnO₂ from MnO₂ and the subsequent formation of Mn2O3 from Zn/MnO₂. The reduction peak at 0.62 V indicates the formation of Mn and Li20. Additionally, during the first cycle, an oxidation peak is observed at 1.38 V, representing the oxidation of Mn to Mn2O3, followed by further oxidation to MnO₂. In the initial cycle, both oxidation and reduction peaks are shifted to higher voltages, which can be explained by the formation of a stable solid electrolyte interface (SEI) layer on the material's surface due to the irreversible decomposition of the electrolyte during the first discharge [33].

In subsequent cycles, the material undergoes an activation process, forming more active sites, as evidenced by the increased current peak of the oxidation peak in the (Figure 10a). In later cycles, the CV curves for the second and third cycles overlap significantly, indicating good stability and reversibility of the GO-20 electrode material. To further explore the reaction mechanism

during charge and discharge, (Figure 10b) shows the charge-discharge curves of the GO-20 anode material over the first three cycles. We observe that the initial discharge specific capacity of the GO-20 electrode material is approximately 1894.7 mA h $\rm g^{-1}$, while the initial charge specific capacity is only 1396.5 mA h $\rm g^{-1}$, resulting in a first Coulombic efficiency of just 73.71%. This substantial capacity loss is due to the large specific surface area of the GO-20 anode material, leading to the irreversible

decomposition of the electrolyte on the electrode surface and the formation of a significant amount of the SEI film [44]. Additionally, the accumulation of some irreversible amorphous ${\rm LiO}_2$ also contributes to considerable lithium loss [54]. Notably, after the first charge and discharge, the charge-discharge curves largely overlap, demonstrating good stability of the GO-20 anode material, consistent with the results of the cyclic curves.

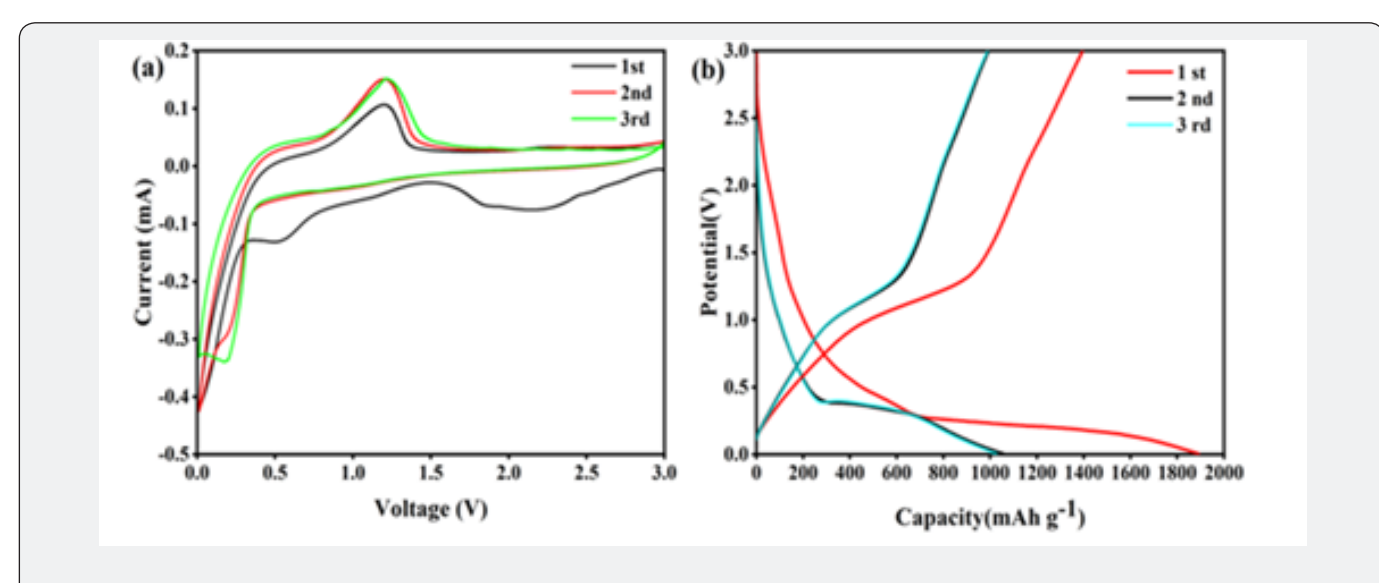


Figure 10: (a) Cyclic voltammetry curves and (b) constant current charge-discharge curves of the GO-20 electrode material for the first three cycles.

To gain a deeper understanding of the fundamental reasons for the improved kinetic performance of the GO-20 anode material, EIS tests were conducted using an electrochemical workstation CH1600E over a frequency range of 0.01 kHz to 100 kHz. This was done to analyze the electrochemical impedance of Zn-3 and GO-20 samples. By fitting the equivalent circuit, the test results of the Zn-3 and GO-20 electrode materials were processed, as shown in (Figure S4). Upon observing the Nyquist plots, it was found that the charge transfer resistance of GO-20 was smaller, because the semicircle diameter in the high-frequency region for the GO-20 electrode material was less than that of the Zn⁻³ electrode material. The superiority of this composite material lies in its unique structure, where graphene serves as a conductive framework, facilitating close contact between different parts of the composite and forming good contact with the current collector. This structural design improves the electronic conductivity of the electrode material by effectively reducing the charge transfer resistance within the material.

As a result, during electrochemical reactions, the composite graphene oxide contributes to faster electron transfer, thereby enhancing the battery's performance and cycling stability. (Figure S5a) shows the TGA curve of GO-20 as the temperature rises from room temperature to 800°C. As the temperature increases from 25°C, a slight weight loss of 3.6% is observed between 25°C

and 150°C. This weight loss is due to the evaporation of water molecules adsorbed on the material's surface as the temperature increases. As the temperature continues to rise to 490°C, an additional 20.5% weight loss is observed, attributed to the reaction of graphene oxide with oxygen at high temperatures producing carbon dioxide, corresponding to the loss of graphene. From 490°C until the end of the experiment, the curve remains essentially flat, indicating no further weight loss, which is attributed to MnO₂. Thus, this result aligns with the 20% graphene oxide content added in the synthesis of the GO-20 material. (Figure S5b) shows the N2 adsorption/desorption isotherm curves of the GO-20 composite. The specific surface area of GO-20 can be used to explore its impact on the kinetic performance of the electrode material and the initial Coulombic efficiency. It was found that the BET specific surface area of the GO-20 composite is approximately 149.76 m²/g⁻¹. A larger specific surface area plays a crucial role in electrochemical energy storage. It provides more active sites for the electrode, which can facilitate effective reactions between the electrolyte and the electrode material, thereby significantly increasing the battery's specific capacity. Additionally, having a larger specific surface area also helps improve the electrochemical kinetic properties of the electrode material, allowing the battery to achieve faster charge-discharge rates. By reasonably controlling the specific surface area, batteries can achieve higher efficiency and reliability while balancing performance and stability.

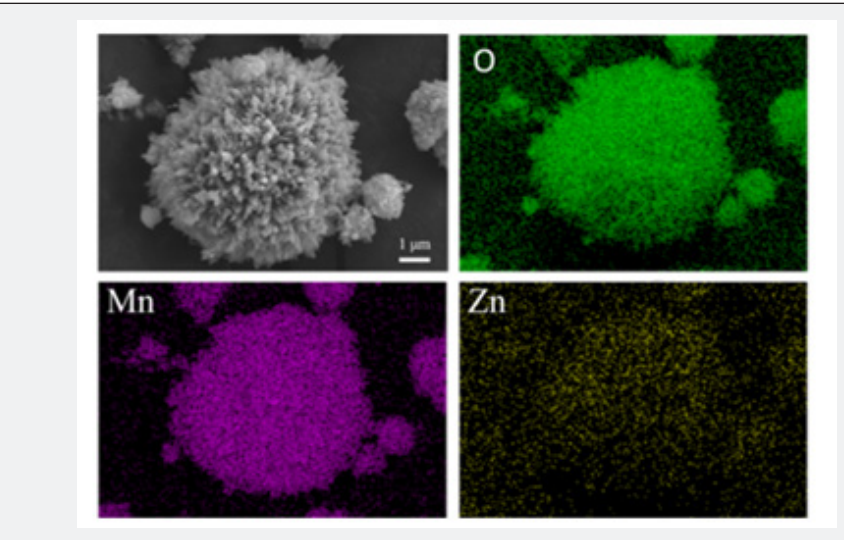


Figure S1: EDS elemental distribution images of hollow sea urchin-like Zn-3/MnO2 nanomaterials.

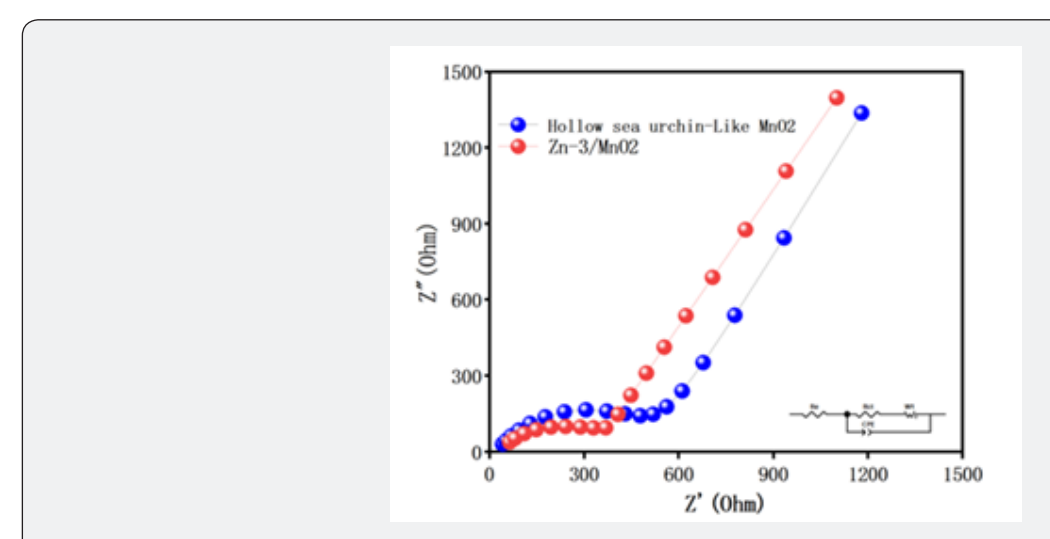


Figure S2: Electrochemical impedance spectra of hollow sea urchin-like MnO2 electrode material and Zn-3 electrode material.

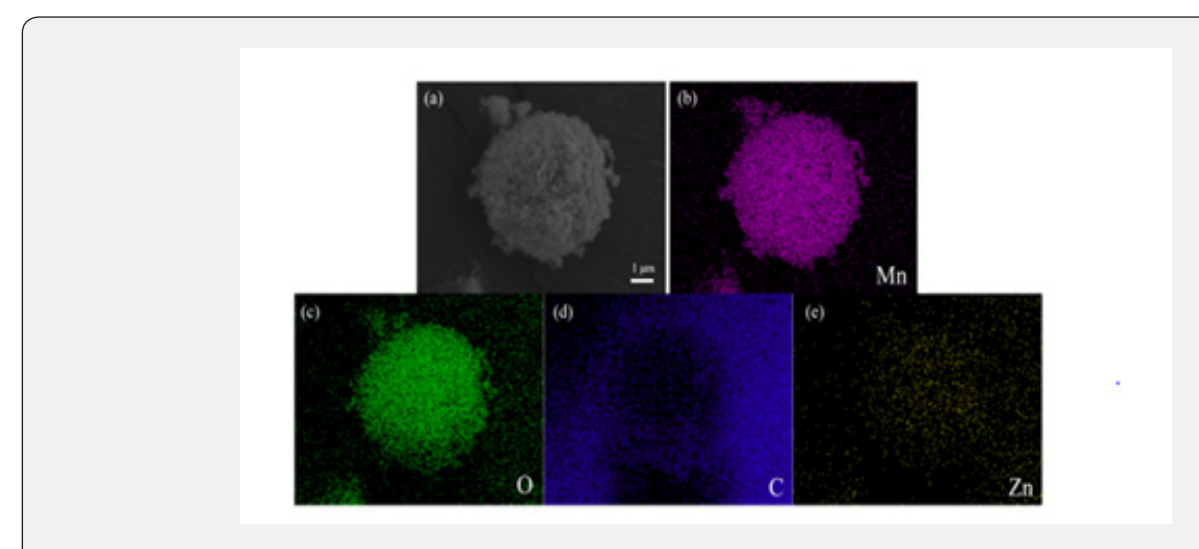


Figure S3: Surface mapping of the GO-20 composite material.

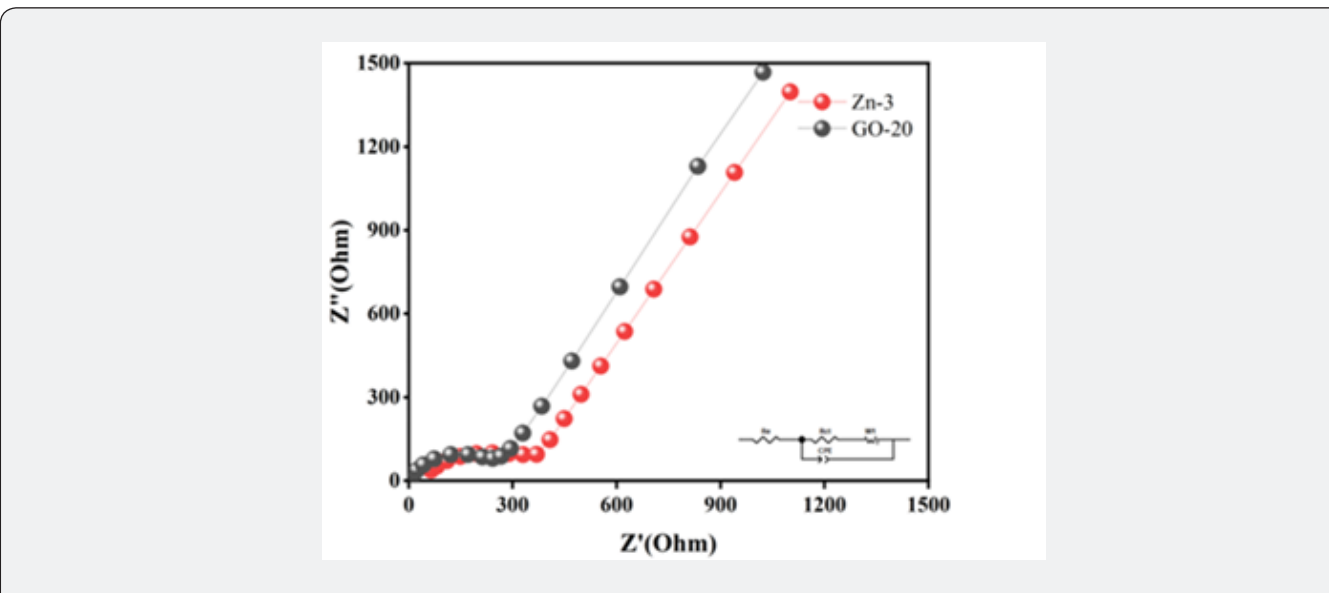


Figure S4: Shows the electrochemical impedance spectra of the GO-20 and Zn-3 electrode materials.

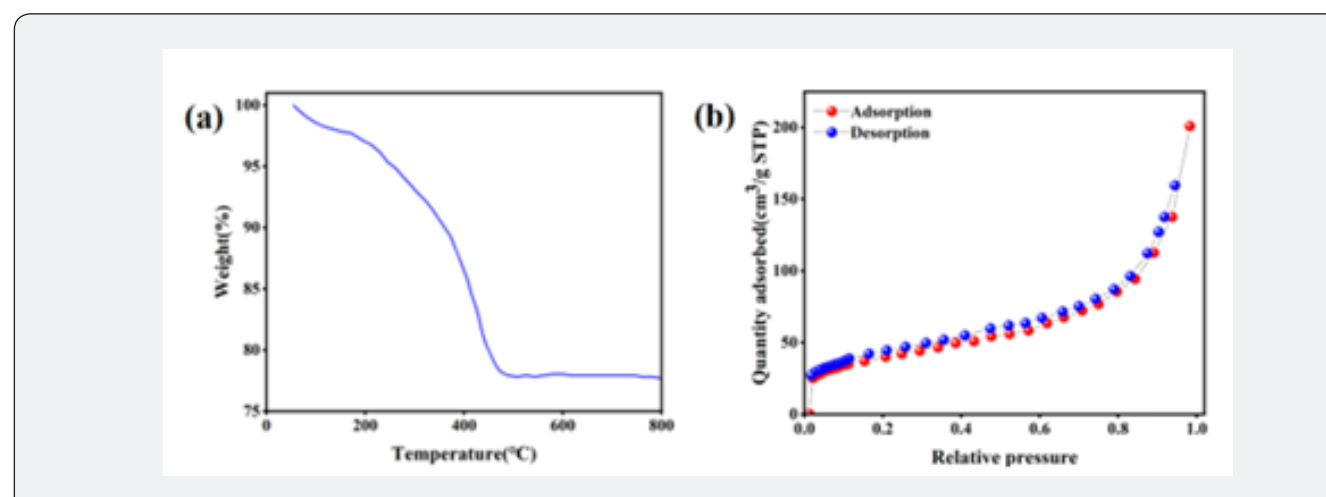


Figure S5(a): Thermogravimetric curve of the Zn-3/MnO2@GO-20 composite; (b): Nitrogen adsorption/desorption isotherm curve of the GO-20 composite.

Table S1: Elemental composition of hollow sea urchin-like Zn⁻³/MnO₂ nanomaterials

nationatoriale.		
Element	Wt%	At%
0	33.95	59.09
Mn	58.36	31.82
Zn	7.69	9.09
Total	100.00	100.00

Experimental

Synthesis of Zn2+-doped Hollow Urticina-like MnO_2 Nanomaterials

First, 0.683 g of $\rm MnSO_4 \cdot H_2O$, 1.0868 g of K2S2O8, and 4 mL of concentrated sulfuric acid were weighed and dissolved in 76

mL of deionized water. Then, 0.09877 g of Zn (CH3COO)2·2H2O was added, and the mixture was stirred thoroughly for 10 minutes to form a uniform solution. Next, the solution was transferred to a stainless-steel autoclave lined with polytetrafluoroethylene (100 mL) and reacted in an oven at 110 °C for 6 hours. After the reaction, the autoclave was allowed to cool naturally to room temperature, and the precipitate was collected. The precipitate was washed three times with deionized water and anhydrous ethanol to remove impurities. Finally, the obtained solid product was dried in a vacuum drying oven at 80°C for 12 hours. The dried samples were then thoroughly ground in a mortar to ensure complete dispersion. To investigate the effect of zinc ion doping content on the hollow sea urchin-like $\rm MnO_2$ nanomaterials, the masses of Zn (CH3COO)2·2H2O added were set to 0.0 g, 0.03292 g, 0.09877 g, and 0.16462 g, corresponding to molar ratios of zinc

ions to manganese ions of 0%, 1%, 3%, and 5%, respectively. All samples were designated as Zn-0, Zn⁻¹, Zn⁻³, and Zn⁻⁵.

Preparation of Zn⁻³/MnO₂ Composite GO Nanomaterials

The procedure involves weighing Zn-3/MnO2 nanoparticles and graphene oxide (GO) in specific mass ratios, where graphene oxide constitutes 10%, 20%, and 30% of the total sample mass. When preparing the solution, the concentration of graphene oxide is maintained at 1 mg/mL. The mixture is subjected to ultrasonic treatment for 2 hours to ensure uniform dispersion of Zn-3/MnO₂ nanoparticles. The mixed solution is then transferred to a sealed 100 mL Teflon-lined autoclave and heated to 90°C for a continuous reaction lasting 36 hours. After the hydrothermal reaction, the autoclave is cooled to room temperature, and the mixture is washed multiple times with alcohol and deionized water. Centrifugation is used to obtain the Zn-3/MnO2@GO composite material from the process. Finally, the solid product is dried in a vacuum oven at 60°C for 12 hours, and the dried sample is thoroughly ground to achieve full dispersion. The samples with different graphene oxide contents are named GO-10, GO-20, and GO-30, respectively.

Materials characterization

The crystal structure of sample was characterized by X-ray diffraction (XRD) on a Rigaku-D/max-2004 with Cu K α radiation (=1.5406 Å) in a scan range from $10^{\rm o}$ to $80^{\rm o}$. The JSM-6700F field emission scanning electron microscopy (SEM) was used at 5 kV voltage to characterize the morphology and microstructure of materials. The elemental species and valence states in sample were confirmed by X-ray photoelectron spectroscopy spectra (XPS) with Thea Probe AR-XPS System. The content of GO in sample was identified by the thermogravimetric analysis (TG) on the STA 449F3. The Brunauer-Emmett-Teller (BET) method was used to analysis the specific surface area of sample.

Electrochemical measurements

The CR2032-type coin half-cells were assembled in an argon atmosphere to test the electrochemical properties of anode materials. The working electrode of half-cells was prepared by mixing anode materials, conductive additive and polyvinylidene difluoride (PVDF) binder with a weight ratio of 7:2:1 in the N-methyl-2-pyrrolidene (NMP) solvent. The as-prepared slurry mixture was uniformly coated onto Cu foil. The areal density of the active materials in the electrodes was approximately 1 mg cm-2. The electrolyte was consisted of LiPF6 solution of ethylene carbonate (EC) and dimethyl carbonate (DMC) (1:1 by volume). The charge-discharge tests were performed within 0.01-3.0 V on a battery testing system (LAND 2001 CT). The electrochemical impedance spectroscopy (EIS) within the frequency range from 0.01 Hz to 100 kHz and cyclic voltammetry (CV) was tested at a scan rate of 0.1 mV s-1 within 0.001-3.0 V on the CHI660D. The galvanostatic intermittent titration technique (GITT) measurements were investigated with current pulse for 30 min

and relaxation of 60 min on LAND 2001 CT.

Conclusion

In this study, a simple one-step hydrothermal method was used to synthesize Zn/MnO2 samples with different zinc ion doping levels. Electrochemical performance tests on the obtained samples showed that the Zn2+-doped samples exhibited superior cycling stability and rate performance compared to the undoped Zn-0 samples. The hollow sea urchin-like MnO₂ electrode material with a Zn²⁺ doping level of 3% showed the best performance, maintaining a discharge specific capacity of 707.6 mA h g⁻¹ after 100 charge-discharge cycles, with no significant capacity decay during the process. Its rate performance was also enhanced compared to the undoped sample. To further enhance the stability and kinetic performance of the Zn/MnO2 electrode material, Zn/ MnO₂@GO composites were synthesized by combining with graphene oxide. The study results showed that the GO-20 anode material maintained a stable capacity of 915.3 mA h g-1 after 100 cycles at a 0.1 C current density. In contrast, the GO-0 anode material stabilized at 707.6 mA h g⁻¹ under the same conditions, indicating that the GO-20 anode material exhibited more stable capacity and improved rate performance during cycling. Further analysis revealed that the synergistic effect of Zn2+ and the combination with graphene oxide, known for its stability and excellent conductivity, further enhanced the conductivity and stability of the anode material. The composite of GO with Zn/MnO₂ further improved its electrochemical performance. Research results indicated that when the graphene oxide content is approximately 20%, the GO-20 anode material demonstrated optimal electrochemical performance, with improvements in both capacity and stability.

References

- Shobana M K (2019) Metal oxide coated cathode materials for Li ion batteries - A review. Journal of Alloys and Compounds 802: 477-487.
- Bedoya-Lora FE, Hankin A, Kelsall GH (2019) Hydrogen sulfide splitting using solar energy and hematite photo-anodes. Electrochimica Acta 317: 384-397.
- Murshed M (2023) Efficacies of technological progress and renewable energy transition in amplifying national electrification rates: contextual evidence from developing countries. Utilities Policy 81: 101512-101521.
- Halkos GE, Gkampoura EC (2020) Reviewing usage, potentials, and limitations of renewable energy sources. Energies 13(11): 2906-2924.
- Banerjee H, Morris A J (2025) Theoretical approaches to study degradation in Li-ion battery cathodes: Crucial role of exchange and correlation. Journal of Materials Research 40(1): 2-35.
- 6. Zhao Y, Li X, Yan B (2016) Recent developments and understanding of novel mixed transition-metal oxides as anodes in lithium-ion batteries. Advanced Energy Materials 6(8): 1502175.
- 7. Krishan O, Suhag S (2019) An updated review of energy storage systems: Classification and applications in distributed generation power systems incorporating renewable energy resources. International Journal of Energy Research 43(12): 6171-6210.

- Maradin D (2021) Advantages and disadvantages of renewable energy sources utilization. International Journal of Energy Economics and Policy 11(3): 176-183.
- Wang Y, Liu B, Li Q. (2015) Lithium and lithium-ion batteries for applications in microelectronic devices: A review. Journal of Power Sources 286: 330-345.
- 10. Wu S, Fan K, Wu M (2016) Two-dimensional MnO₂/graphene hybrid nanostructures as anode for lithium-ion batteries. International Journal of Modern Physics B 30 (27): 1650208.
- 11. Nitta N, Wu F, Lee JT (2015) Li-ion battery materials: present and future. Materials Today 18(5): 252-264.
- Zhou Q, Li Q, Liu S (2021) High Li-ion conductive composite polymer electrolytes for all-solid-state Li-metal batteries. Journal of Power Sources 482: 228929.
- 13. Yokwana K, Ntsendwana B, Nxumalo E N (2023) Recent advances in nitrogen-doped graphene oxide nanomaterials: Synthesis and applications in energy storage, sensor electrochemical applications and water treatment. Journal of Materials Research 38(13): 3239-3263.
- 14. Liu Z, Li R, Deng T (2023) Optimized electrolyte design for improved mechanical stability of NCM523/Gr batteries at 4.6V cycles. Journal of Materials Research 38(21): 4795-4804.
- 15. Zhang L, Chen C (2011) Electrode Materials for Lithium Ion Battery . Progress in Chemistry 23(2-3): 275-283.
- 16. Liu J, Yuan M, Xie T (2022) Ultrathin-ZrO₂-coated LiNi0.4Co0.2Mn0.4O₂ cathode material for Li-ion batteries: Synthesis and electrochemical performance. Journal of Materials Research 37(5): 1019-1029.
- 17. Yang J Wang T, Du C (2019) Overview of the modelling of lithium-ion batteries. Energy Storage Science and Technology 8(1): 58-64.
- Wang DW, Li F, Liu M (2008) 3D aperiodic hierarchical porous graphitic carbon material for high-rate electrochemical capacitive energy storage. Angewandte Chemie-International Edition 47(2): 373-376.
- 19. Qi W, Shapter J G, Wu Q (2017) Nanostructured anode materials for lithium-ion batteries: principle, recent progress and future perspectives. Journal of Materials Chemistry A5 (37): 19521-19540.
- Lu Y, Yu L, Lou XW (2018) Nanostructured conversion-type anode materials for advanced lithium-ion batteries. Chem 4(5): 972-996.
- 21. Yu J, Chen X, Wang Hg (2022) Conjugated ladder-type polymers with multielectron reactions as high-capacity organic anode materials for lithium-ion batteries. Science China-Materials 65(9): 2354-2362.
- Zhou Q, Li Q, Liu S (2021) High Li-ion conductive composite polymer electrolytes for all-solid-state Li-metal batteries. Journal of Power Sources 482: 228929.
- 23. Zhang Y, Chen P, Wang Q (2021) High-capacity and kinetically accelerated lithium storage in ${\rm MoO_3}$ enabled by oxygen vacancies and heterostructure. Advanced Energy Materials 11(31): 2101712.
- 24. Lu L, Li J, Lan L (2018) Research progress of transition metal oxide cathode material. New Chemical Materials 46(9): 65-68.
- 25. Ju GK, Tao ZL, Chen J (2017) Controllable preparation and electrochemical performance of self-assembled microspheres of α -MnO $_2$ Nanotubes. Acta Physico-Chimica Sinica 33(7): 1421-1428.
- 26. Wu J, Raza W, Wang P (2022) Zn-doped ${\rm MnO}_2$ ultrathin nanosheets with rich defects for high performance aqueous supercapacitors. Electrochimica Acta 418: 140339.
- 27. Jia T, Chen J, Deng Z (2014) Facile synthesis of Zn-doped SnO₂ dendrite-

- built hierarchical cube-like architectures and their application in lithium storage. Materials Science and Engineering B-Advanced Functional Solid-State Materials 189: 32-37.
- 28. Tang L, Ji X, Luo H (2020) Achievement of high durability of $\delta\textsc{-MnO}_2$ based pseudocapacitive electrode enabled by Zn doping induced reattachment. Journal of Alloys and Compounds 834: 155117.
- 29. Hao J, Liu Y, Shen H (2016) Effect of nickel-ion doping in $\rm MnO_2$ nanoneedles as electrocatalyst for the oxygen reduction reaction. Journal of Materials Science-Materials in Electronics 27(6): 6598-6605.
- 30. Sun L, Xie J, Zhang X (2020) Controllable synthesis of nitrogen-doped carbon nanobubbles to realize high-performance lithium and sodium storage. Dalton Transactions 49(44): 15712-15717.
- 31. He T, Zeng X, Rong S (2020) The controllable synthesis of substitutional and interstitial nitrogen-doped manganese dioxide: the effects of doping sites on enhancing the catalytic activity. Journal of Materials Chemistry 8(17): 8383-8396.
- 32. Hu Z, Xiao X, Chen C (2015) Al-doped α -MnO $_2$ for high mass-loading pseudocapacitor with excellent cycling stability. Nano Energy 11: 226-234.
- 33. Li J, Ren Y, Wang S (2016) Transition metal doped MnO_2 nanosheets grown on internal surface of macroporous carbon for supercapacitors and oxygen reduction reaction electrocatalysts. Applied Materials Today 3: 63-72.
- 34. Chen X, Ruan P, Wu X (2022) Crystal structures, reaction mechanisms, and optimization strategies of MnO₂ cathode for aqueous rechargeable zinc batteries. Acta Physico-Chimica Sinica 38(11): 2111003.
- 35. Cetinkaya T, Akbulut H, Tokur M (2016) High-capacity Graphene/ α -MnO $_2$ nanocomposite cathodes for Li-O $_2$ batterie. International Journal of Hydrogen Energy 41(23): 9746-9754.
- 36. Khan Z, Park S, Hwang SM (2016) Hierarchical urchin-shaped α -MnO $_2$ on graphene-coated carbon microfibers: a binder-free electrode for rechargeable aqueous Na-air battery. Npg Asia Materials 8: e294.
- 37. Zhang Y, Liu H, Zhu Z (2013) A green hydrothermal approach for the preparation of graphene/ α -MnO $_2$ 3D network as anode for lithium-ion battery. Electrochimica Acta 108: 465-471.
- 38. Yu A, Park HW, Davies A (2011) Free-standing layer-by-layer hybrid thin film of graphene-MnO₂ nanotube as anode for lithium-ion batteries. The Journal of Physical Chemistry Letters 2(15): 1855-1860.
- Ji T-h, Sun M, Han P (2013) A review of the preparation and applications of graphene/semiconductor composites. New Carbon Materials 28(6): 401-407.
- 40. Bian SW, Xu LL, Guo MX (2016) Fabrication of Graphene/Cotton and MnO₂/Graphene/Cotton composite fabrics as flexible electrodes for electrochemical capacitors. Acta Physico-Chimica Sinica 32(5): 1199-1206.
- 41. Reddy MV, Rao GVS, Chowdari BVR (2013) Metal oxides and oxysalts as anode materials for li ion batteries. Chemical Reviews 113(7): 5364-5457.
- 42. Zahan M, Podder J (2020) Role of Fe doping on structural and electrical properties of ${\rm MnO}_2$ nanostructured thin films for glucose sensing performance. Materials Science in Semiconductor Processing 117: 105109.
- 43. Yang Y, Shao T, Zhang Y (2023) Anionic S-doping of a ${\rm ZnMn_2O_4/CNTs}$ cathode material enhances its ${\rm Zn^{2^+}}$ storage performance in aqueous zinc-ion batteries. Journal of Power Sources 564: 232863.

- 44. Rajagopal R, Ryu KS (2020) Morphologically engineered cactus-like MnO₂ nanostructure as a high-performance electrode material for energy-storage applications. Journal of Energy Storage 32: 101880.
- 45. Wang M, Zhao G, Bai X (2023) Gradient concentration refilling of N stabilizes oxygen vacancies for enhanced Zn²⁺ storage. Advanced Energy Materials 13(38): 1730.
- 46. Liu B, Jiang K, Zhu K (2022) Cable-like polyimide@carbon nanotubes composite as a capable anode for lithium-ion batteries. Chemical Engineering Journal 446: 137208.
- Chen X, Huang Y, Zhang X (2015) Graphene supported ZnO/CuO flowers composites as anode materials for lithium-ion batteries. Materials Letters 152: 181-184.
- Quan Chao Z, XiaoYong FAN, JinMei XU (2006) Electrochemical impedance delithiation of spinel spectroscopic study of the first lithium manganese Oxide. Acta Physica-Chimica Sinica 22(2): 234-238.
- 49. Chung SH, Wu YH, Tseng YH (2023) High entropy oxide (CrMnFeNiMg)304 with large compositional space shows long-term

- stability as cathode in lithium-sulfur batteries. Chemsuschem 16(8): 135.
- 50. Ma Y, Zhu Y, Lei Y (2023) Three-dimensional bacterial cellulose and MOF-74 derivatives as anode for high performance potassium-ion batteries. Journal of Alloys and Compounds 946: 169365.
- 51. Liu G, Zhang T, Li X (2023) MoS2@C with S vacancies vertically anchored on V2C-MXene for efficient lithium and sodium storage [J]. Inorganic Chemistry Frontiers 10(5): 1587-1602.
- 52. Singu BS, Hong SE, Yoon KR (2016) Chemical synthesis of seaurchin shaped 3D-MnO2 nano structures and their application in supercapacitors. Journal of Nanoscience and Nanotechnology 16(6): 6093-6101
- 53. Ma C, Jiang J, Xu T (2018) Freeze-Drying-Assisted synthesis of porous SnO₂/rGO xerogels as anode materials for highly reversible lithium/ sodium storage. Chemelectrochem 5(17): 2387-2394.
- 54. Li J, Hwang S, Guo F (2019) Phase evolution of conversion-type electrode for lithium-ion batteries. Nature Communications 10: 2224.



This work is licensed under Creative Commons Attribution 4.0 License DOI: 10.19080/AJOP.2025.06.555697

Your next submission with Juniper Publishers will reach you the below assets

- Quality Editorial service
- Swift Peer Review
- · Reprints availabilitya
- · E-prints Service
- Manuscript Podcast for convenient understanding
- · Global attainment for your research
- Manuscript accessibility in different formats (Pdf, E-pub, Full Text, Audio)
- · Unceasing customer service

Track the below URL for one-step submission

https://juniperpublishers.com/online-submission.php